

Optical Spectroscopy in CoO: Phonons, Electric, and Magnetic Excitations

Ch. Kant,¹ T. Rudolf,¹ F. Schrettle,¹ F. Mayr,¹ J. Deisenhofer,¹ P. Lunkenheimer,¹ M. V. Eremin,^{1,2} and A. Loidl¹

¹*Experimental Physics V, Center for Electronic Correlations and Magnetism,
University of Augsburg, 86135 Augsburg, Germany*

²*Kazan State University, 420008 Kazan, Russia*

(Dated: November 12, 2018)

The reflectivity of single-crystalline CoO has been studied by optical spectroscopy for wave numbers ranging from 100 to 28,000 cm^{-1} and for temperatures $8 < T < 325$ K. A splitting of the cubic IR-active phonon mode on passing the antiferromagnetic phase transition at $T_N = 289$ K has been observed. At low temperatures the splitting amounts to 15.0 cm^{-1} . In addition, we studied the splitting of the cubic crystal field ground state of the Co^{2+} ions due to spin-orbit coupling, a tetragonal crystal field, and exchange interaction. Below T_N , magnetic dipole transitions between the exchange-split levels are identified and the energy-level scheme can be well described with a spin-orbit coupling $\lambda = 151.1$ cm^{-1} , an exchange constant $J = 17.5$ cm^{-1} , and a tetragonal crystal-field parameter $D = -47.8$ cm^{-1} . Already in the paramagnetic state electric quadrupole transitions between the spin-orbit split level have been observed. At high frequencies, two electronic levels of the crystal-field-split d -manifold were identified at 8,000 and 18,500 cm^{-1} .

PACS numbers: 78.30.Am, 63.20.kk, 75.50.Ee, 71.70.Ej

I. INTRODUCTION

Strongly correlated transition metal compounds with partly filled d bands display a variety of properties, interesting for fundamental research and important for future technological applications: Colossal magnetoresistance and multiferroicity in the manganites, high-temperature superconductivity in the cuprates, exotic superconductivity in the ruthenates and the cobaltites are illuminating examples. The complexity of the ground state is driven by strong electronic correlations and a strong interplay between charge, orbital, spin, and lattice degrees of freedom. In many of these compounds, orbital degrees of freedom play an essential role and access to the orbital state can be obtained by studying the splitting of the d levels, which can reveal the effects of the crystal-field (CF), spin-orbit coupling (SOC), and exchange-coupling in the magnetically ordered state. However, experimental methods to study these local d - d excitations are limited. They are electric dipole forbidden and, hence, very weak when compared to Mott-Hubbard ($d^n d^n - d^{n-1} d^{n+1}$) or charge transfer excitations ($d^n d^n - d^{n+1} L^-$), which sometimes are in a similar energy range. Localized d - d excitations have been analyzed using electron loss spectroscopy¹ and, recently, with the use of nonresonant inelastic X-ray scattering Larson *et al.*² determined the energy scale of d - d excitations within the charge transfer gaps of NiO and CoO. The latter results have been quantitatively explained using a local many body approach by Haverkort *et al.*³ Note that the late transition metal monoxides are prototypical correlated electron systems and benchmark materials for charge-transfer insulators.⁴

Moreover, transition metal monoxides are regarded as model systems for spin-phonon coupling effects. The idea of a purely magnetic-order-induced phonon splitting has been put forth by Massidda *et al.*⁵ for the antiferromag-

netic (AFM) transition metal monoxides and has been further substantiated in a recent work by Luo *et al.*⁶ The splitting of the transverse optic modes below the Néel temperature T_N has indeed been experimentally documented by Chung *et al.*⁷ in MnO and NiO by inelastic neutron scattering and by Rudolf *et al.*⁸ in MnO by infrared spectroscopy. The splitting of phonon modes has also been observed in a number of spinel compounds at the onset of AFM order,^{9,10,11} and has been interpreted in terms of a spin-driven Jahn-Teller (JT) effect.^{12,13}

The purpose of this study is to reinvestigate the optical properties of CoO by infrared (IR) spectroscopy with regard to spin-phonon coupling effects and d - d excitations. CoO has first been synthesized by Klemm and Schüth.¹⁴ Magnetic susceptibility measurements^{15,16,17,18,19} show an antiferromagnetic transition at approximately 290 K with a negative Curie-Weiss temperature of the order of the AFM transition temperature. The onset of magnetic order is accompanied by a structural phase transition with a small tetragonal distortion.²⁰ At room temperature CoO is paramagnetic and exhibits the cubic NaCl structure (space group $\text{Fm}\bar{3}\text{m}$; $a = 0.42495$ nm) while at 92 K the lattice parameters of the tetragonal cell are $a = 0.42552$ nm and $c/a = 0.9884$. Later on, low temperature X-ray diffraction experiments revealed a rhombohedral distortion in addition to the tetragonal distortion,²¹ while high-resolution synchrotron powder diffraction even manifested a monoclinic symmetry (space group $\text{C}2/\text{m}$) of antiferromagnetic CoO.²² The spin structure of CoO in the AFM state has been determined by neutron scattering diffraction by Shull *et al.*²³ On the basis of these data it has been concluded that the magnetic moments in CoO are arranged in ferromagnetic (111) planes with the preferred spin direction along $[\bar{1}\bar{1}7]$, which is intermediate to the (111) plane and the tetragonal axis.²⁴ However, there has been some dispute about the true magnetic structure and possible multi spin

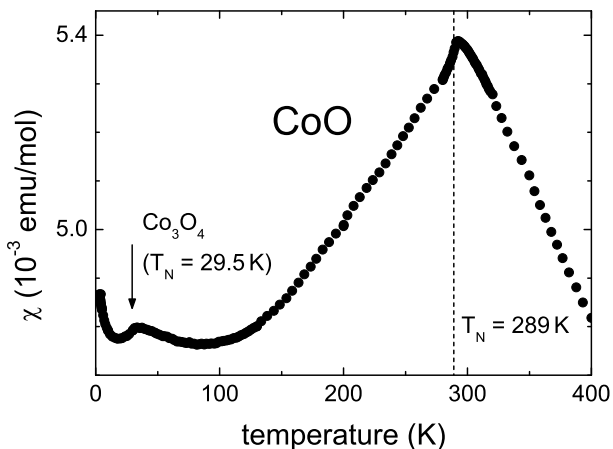


FIG. 1: Temperature dependent susceptibility of a single crystalline CoO platelet, with the external magnetic field directed perpendicular to the (111) plane. The measurement was performed at an external magnetic field $\mu_0 H = 0.1$ T. The magnetic ordering temperature of the impurity phase Co_3O_4 is indicated by an arrow.

configurations occurring in CoO.^{25,26,27,28} Although previous absorption measurements reported the observation of $d-d$ excitations in the paramagnetic (PM) as well as in the AFM state,^{29,30,31,32} a comprehensive and unambiguous description of the splittings and determination of the relevant interaction parameters is still missing. We are able to describe the observed splittings in the PM and antiferromagnetically ordered state very well by taking into account SOC, tetragonal crystal field, and exchange splitting contributions.

II. EXPERIMENTAL DETAILS AND SAMPLE CHARACTERIZATION

High quality single crystals with optical quality (space group $\text{Fm}\bar{3}\text{m}$, $a = 0.425$ nm at room temperature) in the form of platelets with dimensions of approximately 1 cm^2 and 1 mm thickness were purchased from MaTecK GmbH. Impurities like Fe or Ni were less than 0.01%. For characterization, the magnetic properties were studied using a commercial SQUID magnetometer (Quantum Design MPMS-5) with external magnetic fields up to 50 kOe. The heat capacity was measured in a Quantum Design Physical Properties Measurement System for temperatures from $2 < T < 300$ K. The dielectric properties were determined using a frequency-response analyzer (Novocontrol) at frequencies between 1 Hz and 1.5 MHz.³³ For these measurements silver-paint contacts were applied to opposite sides of the platelets. The reflectivity measurements were carried out using the Bruker Fourier-Transform Spectrometers IFS 113v and IFS 66v/S, which both are equipped with a He-flow (4 - 600 K) cryostat. Using different light sources, different beam splitters and different detectors, we were able to

cover the frequency range from 100 cm^{-1} to $28,000 \text{ cm}^{-1}$. For the analysis of our reflectivity spectra, we derived the complex dielectric constant or the complex index of refraction by means of Kramers-Kronig transformation with a constant extrapolation towards low frequencies and a smooth power law extrapolation at high wave numbers.

It is known from previous experiments and publications that even high-quality single crystals of CoO can suffer from the intergrowth of Co_3O_4 clusters. It was shown that small impurity-free single crystals could only be obtained by annealing CoO crystals in Co vapor (see Ref. 19). Therefore, we characterized our samples carefully by measuring the magnetic susceptibility, the specific heat, and the dielectric properties. Despite the fact that CoO is a thoroughly studied transition-metal oxide, we found that the information regarding these basic properties is incomplete: The temperature dependence of the magnetic susceptibility of CoO has been studied by Singer¹⁶ between 100 K and 800 K. The broad temperature range of this investigation allowed a rather precise determination of the Curie-Weiss temperature (-330 K) and paramagnetic moment ($5.25 \mu_B$). A careful susceptibility analysis has been reported in Ref. 19. These authors removed nonstoichiometries by heating a small single crystal in Co vapor and also performed measurements under external stress conditions. We are not aware of any detailed investigation of the heat capacity specifically down to low temperatures. Around T_N , it has been investigated in Refs. 34 and 35, the specific heat over a broader temperature range, namely from $100 < T < 500$ K is documented in Refs. 36, 37, and 38. The dielectric permittivity has been published by Rao and Smakula³⁹ measuring the dielectric constant and the dielectric loss of CoO for frequencies between 100 Hz and 1 MHz from liquid nitrogen up to room temperature.

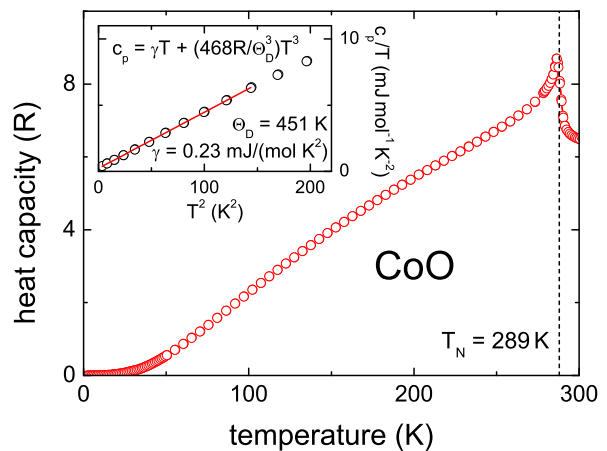


FIG. 2: (Color online) Heat capacity of CoO vs. temperature. Inset: plot of c_p/T vs. T^2 (see text). The best fit of the low temperature specific heat is achieved taking into account a small linear term $\gamma = 0.23 \text{ mJ}/(\text{mol K}^2)$ (solid line in inset).

Figure 1 shows the temperature dependence of the magnetic susceptibility as measured in an external field of $\mu_0 H = 0.1$ T for temperatures $2.5 < T < 400$ K, which is in good agreement with previous publications. The measurement was performed at an magnetic field $\mu_0 H = 0.1$ T. The AFM transition appears as a sharp cusp close to 290 K. Below the ordering temperature, the susceptibility decreases before a slight cusp becomes visible close to 30 K, which corresponds to AFM ordering temperature $T_N = 29.5$ K of Co_3O_4 .⁴⁰ Towards lower temperatures we observe an increase below about 20 K which signals a Curie contribution due to free Co spins probably located in grain boundaries or domain walls. Our susceptibility data in the range $350 < T < 400$ K yields a Curie-Weiss temperature of approximately -450 K and an effective moment $p_{\text{eff}} = 5.7 \mu_B$, which have to be compared to $\Theta_{CW} = -330$ K and $p_{\text{eff}} = 5.25 \mu_B$ obtained by Singer.¹⁶ The discrepancy is attributed to the larger temperature range in the PM phase up to 800 K in the latter study, which naturally leads to more reliable parameters. Assuming a spin-only contribution of high-spin Co^{2+} -ions with $S = 3/2$ the effective moment $p_{\text{eff}} = 5.25 \mu_B$ results in an effective g -value $g = 2.71$, which indicates a non-negligible contribution of the orbital momentum.⁴¹

The temperature dependence of the molar heat capacity c_p is documented in Fig. 2. The AFM transition can clearly be seen. From a closer inspection of the anomaly at the AFM ordering we determine a phase-transition temperature $T_N = 289$ K in agreement with our susceptibility data. At room temperature, just above T_N , the heat capacity amounts to approximately $6.5 R$ and is significantly enhanced when compared to a solid with 6 phonon branches, i.e., 2×3 degrees of freedom. This enhanced heat capacity likely results from crystal-field contributions.

At low temperatures the heat capacity can best be fit utilizing a T^3 law and in addition a small linear term. A fit taking into account only data below 12 K, results in a Debye temperature of $\Theta_D = 451$ K (see inset of Fig. 2), which is expected from the phonon dynamics. From the normal modes of vibrations Kushwaha⁴² calculated $\Theta_D(T)$. He found $\Theta_D \approx 500$ K towards 0 K and values approaching 600 K at the Néel temperature, the latter being in good agreement with published experimental results.⁴³ Hence, at low temperatures magnetic contributions seem to play only a minor role in CoO. Obviously, the AFM magnons display a large gap due to strong SOC, which would explain the absence of any dispersive magnon contributions at low temperatures and the enhanced heat capacity at higher temperatures when compared to a non-magnetic solid. This could also explain the small linear term (see inset in Fig. 2). To strengthen these arguments a more detailed analysis including the heat capacity of phonons, magnons, and Schottky-like crystal field levels is necessary but beyond the scope of this paper.

Finally, we also measured the dielectric constant ϵ' and the conductivity σ' of CoO between 4 and 500 K

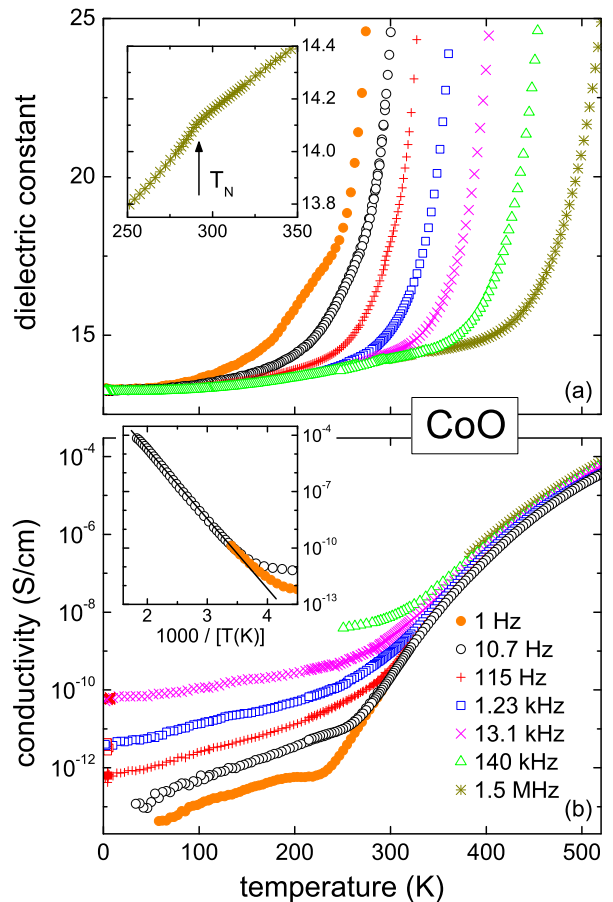


FIG. 3: (Color online) Temperature dependence of the real part of the dielectric constant ϵ' [upper frame: (a)] and real part of the conductivity σ' [lower frame: (b)] of CoO measured at different frequencies between 1 Hz and 1.5 MHz. A (100) platelet has been investigated with the electrical field perpendicular to the (100) plane. The inset in (a) demonstrates the presence of an anomaly in $\epsilon'(1.5 \text{ MHz}) \approx \epsilon_s$ at the magnetic phase transition. The inset in (b) shows the temperature dependence of the dc conductivity in an Arrhenius type presentation. The line corresponds to a band gap of 1.5 eV.

and 1 Hz - 1.5 MHz. The results are documented in Fig. 3. Only below room temperature and for high measuring frequencies f the static dielectric constant is approached, yielding approximately $\epsilon_s = 13$ at low temperatures [Fig. 3(a)]. At high temperatures the real part of the dielectric constant is dominated by ac contributions. It reaches colossal values up to 10^4 (not shown), which may be due to hopping conductivity⁴⁴ or Maxwell-Wagner polarization.⁴⁵ Only for $f = 1.5$ MHz the room temperature value of the static dielectric constant $\epsilon_s = 14.2$ can be estimated. This value is slightly enhanced when compared to published results by Rao and Smakula,³⁹ who found $\epsilon_s = 12.9$ at room temperature. At relatively high measuring frequencies, the AFM ordering is displayed by a small cusp in the temperature-dependent dielectric constant [inset of Fig. 3(a)].

The conductivity σ' of CoO is shown in Fig. 3(b). Here frequency independent *dc* conductivity dominates above room temperature, while *ac* contributions dominate at lower temperatures. As can be read off close to 100 K in the Fig. 3(b), the frequency dependence of the conductivity deviates from a linear behavior and can best be represented by a power law, $\sigma \sim \omega^s$, with $s \sim 0.7$, a typical signature of hopping conduction in disordered solids.⁴⁴ Similar behavior was found in numerous transition-metal oxides (see, e.g., Ref. 46). The inset of Fig. 3(b) shows the *dc* contributions at high temperatures in an Arrhenius type representation. The conductivity can well be described assuming a gap of approximately 1.5 eV, which compares well with published results.³⁹

III. MODEL CALCULATIONS AND ANALYSIS

The reflectivity $R(\omega)$ of an interface is governed by Fresnel's equations. In case of light impinging on a sample surface at normal incident, they can be simplified according to

$$R(\omega) = r(\omega)r^*(\omega) = \left| \frac{\sqrt{\varepsilon(\omega)} - \sqrt{\mu(\omega)}}{\sqrt{\varepsilon(\omega)} + \sqrt{\mu(\omega)}} \right|^2. \quad (1)$$

Here, r is the complex reflectance coefficient, ε the dielectric function and μ the magnetic permeability. In most compounds, μ has negligible influence on the reflectivity spectrum and is usually set to unity in the optical frequency range. Equation (1) is valid for all isotropic, homogeneous, local, and linear materials in the limit of classical electrodynamics.

In order to analyze our reflectivity data, we use model functions for both the dielectric function and the magnetic permeability. The phononic and electronic contributions can be obtained by the factorized dielectric function⁴⁷

$$\varepsilon(\omega) = \varepsilon_\infty \prod_j \frac{\omega_{\text{LO}j}^2 - \omega^2 - i\gamma_{\text{LO}j}\omega}{\omega_{\text{TO}j}^2 - \omega^2 - i\gamma_{\text{TO}j}\omega}, \quad (2)$$

where, in case of the phonon modes, $\omega_{\text{TO}j}$, $\omega_{\text{LO}j}$, $\gamma_{\text{TO}j}$, and $\gamma_{\text{LO}j}$ can be directly interpreted as eigenfrequencies (ω_j) and damping constants (γ_j) of the transversal (TO) and longitudinal (LO) optical modes, respectively. j is an index variable which runs over all phononic and electronic excitations. ε_∞ arises from high-frequency electronic absorption processes beyond the phonon domain. The dielectric strength $\Delta\varepsilon_j$ of excitation j can explicitly be derived from the parameters of the model function if the resonances are well separated:

$$\Delta\varepsilon_j = \varepsilon_\infty \frac{\omega_{\text{LO}j}^2 - \omega_{\text{TO}j}^2}{\omega_{\text{TO}j}^2} \prod_{i \geq j+1} \frac{\omega_{\text{LO}i}^2}{\omega_{\text{TO}i}^2}, \quad (3)$$

The effective ionic plasma frequency Ω_j of each excitation can then be expressed by

$$\Omega_j^2 = \Delta\varepsilon_j \omega_{\text{TO}j}^2. \quad (4)$$

An alternative way to model the dielectric function is by utilizing a sum of Lorentz oscillators:

$$\varepsilon(\omega) = \varepsilon_\infty + \sum_j \frac{\Omega_j^2}{\omega_j^2 - \omega^2 - i\gamma_j\omega} \quad (5)$$

Here, three parameters are adjustable per mode: ω_j and γ_j are eigenfrequency and damping of the j th resonance, respectively. The third fit parameter, which enters Eq. (5), is the plasma frequency Ω_j of mode j . Comparing the model dielectric functions one can deduce that Eqs. (2) and (5) become identical if the damping coefficients of TO and LO modes are equal.

It was shown by Scott⁴⁸ that the following equation holds true for the overall plasma frequency in a multi-mode system:

$$\Omega^2 = \sum_k \Omega_k^2 = \frac{\varepsilon_\infty}{V\varepsilon_{\text{vac}}} \sum_l \frac{(Z_l^*e)^2}{m_l} \quad (6)$$

V denotes the unit-cell volume and Z_l^*e the effective charge of the l th ion with mass m_l contributing to a specific phonon mode. ε_{vac} is the dielectric permittivity of free space.

Our reflectivity data have been analyzed by utilizing Eqs. (1), (2), and (5) and a fit routine which was developed by Kuzmenko.⁴⁹

We also studied phonon eigenfrequencies and damping coefficients as a function of temperature T . To account for purely anharmonic effects, we assume

$$\omega_{\text{TO}j}(T) = \omega_{0j} \left(1 - \frac{c_j}{\exp(\Theta_D/T) - 1} \right) \quad (7)$$

for the temperature dependence of the transverse eigenfrequency $\omega_{\text{TO}j}$ and

$$\gamma_{\text{TO}j}(T) = \gamma_{0j} \left(1 + \frac{d_j}{\exp(\Theta_D/T) - 1} \right) \quad (8)$$

for the temperature dependence of the damping $\gamma_{\text{TO}j}$ of mode j , respectively. ω_{0j} and γ_{0j} are the eigenfrequency and damping of mode j at 0 K. Θ_D denotes the Debye temperature and was treated as a free fitting parameter as well as the constants c_j and d_j , which determine the strength of the anharmonic contributions. Detailed calculations of temperature and frequency dependent anharmonicity can be found in Ref. 50.

IV. RESULTS AND DISCUSSION

Figure 4 presents the reflectivity of CoO between 150 and 28,000 cm^{-1} for different temperatures above and below the antiferromagnetic ordering temperature ($T_N = 289$ K). At room temperature the reflectivity is dominated by a broad reststrahlen band between 300 and 600 cm^{-1} , which is due to the optical phonons of the

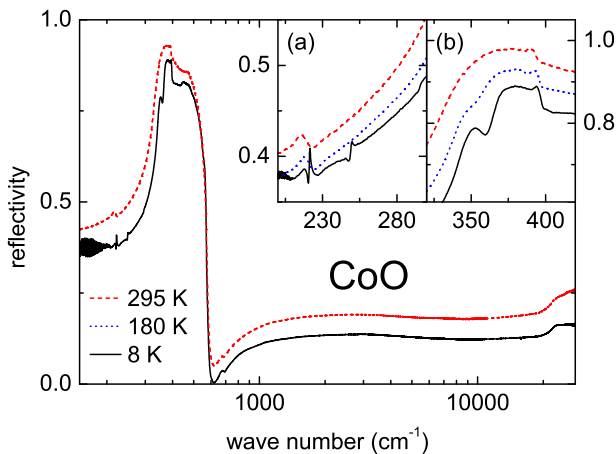


FIG. 4: (Color online) Reflectivity of CoO between 150 and 28,000 cm^{-1} at three different temperatures. The curves in the main frame and inset (b) are successively shifted by an amount of 0.05 for clarity. Inset (a) shows the frequency regime between 200 and 300 cm^{-1} on an expanded scale, while inset (b) provides a closer look in the frequency range between 320 and 420 cm^{-1} , where the splitting of the phonon mode occurs.

NaCl like structure. At zero wave vector the two transverse phonons are degenerate and their eigenfrequencies are determined by the strong increase of the reflectivity close to 300 cm^{-1} . The frequency of the longitudinal optical phonon is determined by the steep decrease of the reflectivity at 600 cm^{-1} . Ideally, the reflectivity in between these two characteristic frequencies, where ϵ' is negative, should be close to unity, at least at low temperatures where anharmonic effects are small. Deviations from this idealized behavior and additional structures usually result from multiple phonon excitations, which will become more pronounced with increasing temperature. The observed structure in the reflectivity on top of the reststrahlen band around 400 cm^{-1} could result from such a two-phonon processes involving zone boundary optical and acoustical modes, which sum up to a zero wave-vector excitation with a dipole moment transferred from the transverse optic phonon mode. Indeed, a weak multi-phonon structure close to 400 cm^{-1} has been calculated by Upadhyay and Singh.⁵¹ However, much stronger peaks in the combined density of states are calculated to appear close to 435, 500, and 535 cm^{-1} , which could not be identified unambiguously. In addition, it has to be stated that the temperature dependence of the observed structures [inset (b) of Fig. 4] is not in accord with anharmonic effects. Multiphonon structures usually become more significant on increasing temperatures, a fact that definitely is not observed in CoO. The inset (b) of Fig. 4 documents that the 400 cm^{-1} anomaly remains almost constant from the lowest to the highest temperatures. Hence, the origin of this structure close to 400 cm^{-1} remains unsettled. In addition to the reststrahlen band due to the phonons, an increase in the reflectivity close

to 22,000 cm^{-1} signals electronic interband transitions.

At first sight, small additional anomalies close to 220 and 700 cm^{-1} can be seen in the frequency-dependent room-temperature reflectivity displayed in Figure 4. On cooling and passing the AFM phase transition no significant shifts or changes are visible, but the appearance of small additional bands close to 250 and 350 cm^{-1} can be detected [see insets (a) and (b) of Fig. 4]. Inset 4(a) also documents that the rather broad feature of the 220 cm^{-1} transition is superimposed by a sharp structure when entering the magnetically ordered phase. The anomaly close to 249 cm^{-1} exhibits a similar shape, namely a dip followed by a peak. Note that weak features also appear at low temperatures at 142 cm^{-1} and 295 cm^{-1} as shown in Fig. 5. The interference fringes at low frequencies are due to the finite thickness of the plan-parallel sample. At this point we would like to state that the anomalies at 142, 220, 249, 295, and close to 700 cm^{-1} are of electronic origin and will be discussed later. The additional band close to 350 cm^{-1} , which evolves just below the magnetic ordering [see inset (b) of Fig. 4], represents the magnetic-order induced phonon splitting.

We converted the reflectivity spectrum into a frequency dependent extinction coefficient κ , which is the imaginary part of the refractive index, in order to reveal the transition features more clearly. The reststrahlen band now roughly corresponds to a loss peak (upper panel of Fig. 5). It splits at low temperatures which becomes nicely visible as a clear double peak structure. An enlarged view of the anomalies between 200 and 300 cm^{-1} is provided in inset (a). Again, at room temperature ($T > T_N$), only one single peak is seen, which we denote as Q_1 in the following. It becomes superimposed by an additional negative cusp at low temperatures. The detailed temperature evolution is shown in the lower panel of Fig. 5. In the following, we label the three negative cusps at 221, 249, and 295 cm^{-1} with $M_2 - M_4$, respectively. These excitations appear below 100 K only, deep in the magnetically ordered state. They increase slightly in intensity and saturate below 25 K, but show no significant shifts in frequency. The inset in the lower panel documents the occurrence of a further excitation (M_1) at 142 cm^{-1} . It behaves similar to $M_2 - M_4$ as it is dip-like and vanishes at approximately 100 K. M_1 strongly resembles the results of infrared absorption by Milward,³⁰ who detected a strong absorption at 142.3 cm^{-1} . Similar findings were revealed in the Raman studies of Hayes and Perry.⁵² This is an experimental evidence, that $M_1 - M_4$ are intrinsic excitations of CoO, since they appear at approximately at the same temperature and show no spectral changes at the ordering temperature of the impurity phase Co_3O_4 . We further see small kinks at 600 and 680 cm^{-1} [inset (b) of Fig. 5], which we will denote as Q_2 and Q_3 , respectively. They reveal almost no temperature dependence and do not coincide with calculated multi-phonon bands.⁵¹

In the following we will first discuss the phonon excitations, before we will turn to the nature of the electronic

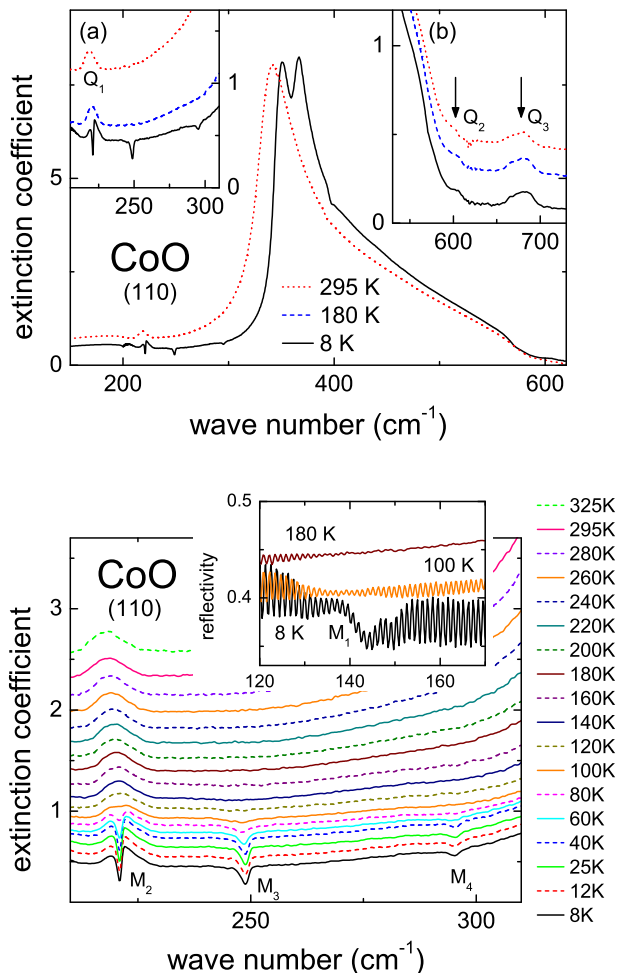


FIG. 5: (Color online) Upper panel: Extinction coefficient κ vs. wave numbers at 8 K and 295 K. The insets show enlarged regions at (205 - 310 cm^{-1}) and (530 - 730 cm^{-1}) wave numbers for κ at 8, 180, and 295 K. The curves in both insets are separated by an amount of 0.2 for clarity. Lower panel: Sequence of temperature dependent measurements of the extinction coefficient vs. wave numbers between 210 and 320 cm^{-1} and for temperatures $8 < T < 325$ K. The data are cumulatively shifted by an amount of 0.1 for clarity. An electric transition close to 220 cm^{-1} is visible already at temperatures above the magnetic phase transition ($T_N = 289$ K). At 100 K magnetic dipole transitions evolve, which gain strength on decreasing temperature. The inset shows an expanded scale of the reflectivity between 120 and 170 cm^{-1} to demonstrate the appearance of a further excitation close to 142 cm^{-1} (see text).

excitations occurring below and above the Neel temperature.

A. Phonon excitations

We tried to fit the reflectivity spectra using a four-parameter fit, but the anomalies on top of the rest-

strahlen band together with the splitting of the phonon modes below T_N did not allow for a satisfactory fitting procedure. Therefore, we transformed the reflectivity into dielectric function and fitted these spectra using a Lorentz fit with three parameters as outlined in Eq. (5). For comparison, we performed four-parameter fits in the paramagnetic phase and found good agreement between the two procedures. The results of the Lorentz fits are plotted in Fig. 6. The upper frame (a) gives the temperature dependence of the TO eigenfrequencies. Assuming that the main distortion occurring below T_N is tetragonal,²⁰ the triply degenerate T_{1u} of the cubic rock-salt structure at room temperature should split into a doublet and a singlet. Such a scenario is in agreement with the observed splitting. The mode with the larger spectral weight at high temperatures smoothly evolves from the cubic room temperature phase and increases from 335.4 cm^{-1} at room temperature to 348.1 cm^{-1} at liquid He temperatures. Just below T_N a second mode splits off with a higher eigenfrequency and increases up to 363.1 cm^{-1} at the lowest temperature. The splitting of the TO modes in CoO hence amounts 15.0 cm^{-1} . We would like to recall, that the low-temperature magnetic phase reveals a monoclinic symmetry⁵⁵ and one certainly can expect a large number of IR active phonons. However, these additional splittings are probably below the experimental resolution ($< \sim 0.5 \text{ cm}^{-1}$). In comparison to MnO, where the overall splitting of the TO mode in the antiferromagnetic state was estimated to be approximately 30 cm^{-1} ,⁸ the splitting is reduced by a factor of two. Since $\Theta_{CW}/T_N \sim 1$ in CoO, one may infer that spin frustration indeed may account for the large magnetic-order induced phonon splitting in MnO.

The temperature dependence of the damping of the transverse phonon modes is shown in Fig. 6(b). The damping of the cubic T_{1u} continuously decreases towards low temperatures and evolves again smoothly into the mode with larger spectral weight below T_N and reaches approximately 12.5 cm^{-1} at low temperatures. Such a behavior is expected for an anharmonic solid and both the temperature dependence of the eigenfrequency and the damping are well described by fits [solid lines in Figs. 6(a) and (b)] according to Eqs. (7) and (8), respectively. The fit yields a Debye temperature of $\Theta_D = 526$ K, an enhanced value compared to the low-temperature

TABLE I: Phonon excitations in CoO observed in the present work, compared to reports in literature. All eigenfrequencies are given in cm^{-1} .

| FIR | | neutron scattering | | |
|-------------|-------------|--------------------|----------|----------|
| (this work) | | Ref. 53 | Ref. 54 | |
| 8 K | 295 K | 295 K | 110 K | 425 K |
| 348.1 (TO1) | 335.7 (TO) | 348.5 (TO) | 348 (TO) | 330 (TO) |
| | 363.1 (TO2) | | | |
| | 562.1 (LO) | 545.5 (LO) | 524 (LO) | |

thermodynamic Debye temperature (see Fig. 2) but comparable to the experimentally determined Debye temperatures at ambient conditions.⁴³ The damping of the second mode below T_N cannot be described by a simple anharmonic behavior.

The temperature dependence of the ionic plasma frequency of the optical modes is shown in Fig. 6(c). Both modes roughly are of equal strength with a value of 700 cm^{-1} from lowest temperatures up to 200 K. On further approaching the phase boundary, the main mode gains weight reaching a value of 990 cm^{-1} , whereas the split-off mode rapidly gets suppressed. Due to the overlap of the two modes and the decreasing weight of the second mode the values above 200 K contain a larger uncertainty.

Finally, the eigenfrequencies and damping constants of the TO and LO modes have also been obtained from a four-parameter fit at room temperature, where only the cubic T_{1u} mode is observable. The TO and LO eigen-

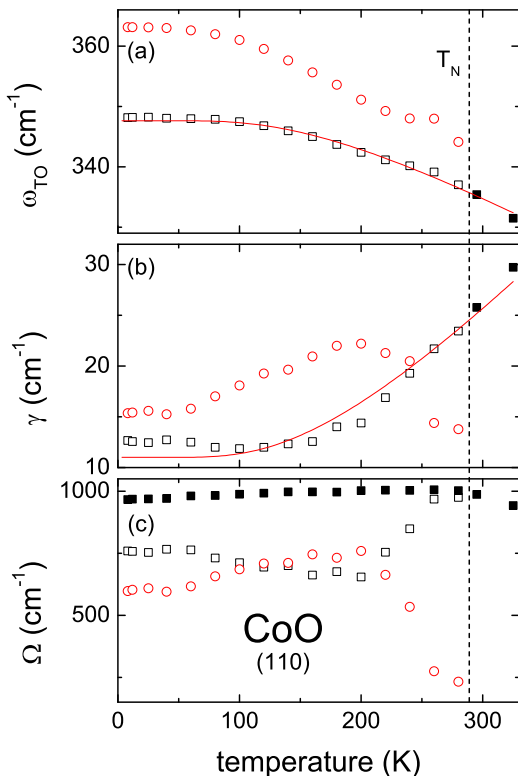


FIG. 6: (Color online) Temperature dependencies of eigenfrequency (a), damping constants (b), and effective ionic plasma frequencies (c) of the transverse optical phonon modes of CoO. The main mode (empty black squares) and the split-off mode, which appears in the antiferromagnetic phase (empty red circles), are shown. All measurements have been performed with single crystalline platelets with the (110) surface close to normal incidence. The solid lines in (a) and (b) were calculated assuming a simple anharmonic model [see Eqs. (7) and (8)]. Black solid squares denote the respective quantity above T_N or in (c) the overall plasma frequency.

frequencies were determined as 335.7 and 562.1 cm^{-1} , respectively. The former value coincides with the one obtained from the Lorentz fit as expected. In Table I these values are compared to the ones reported earlier by Gielisse *et al.*⁵³ and Sakurai *et al.*⁵⁴. The overall agreement seems satisfactory, even though the eigenfrequency of the LO mode of the neutron scattering study is off by almost 8% when compared to our result. However, no longitudinal optical eigenfrequency was reported at room temperature. It should be mentioned that based on the experimental phonon excitations the phonon dynamics of CoO has been calculated using lattice-dynamic models of different complexity^{42,51,56} reaching satisfactory agreement between experimental data and model calculations. In Ref. 51 also a detailed calculation of the two-phonon density of states has been provided. Finally, the lattice dynamics of CoO has recently been calculated from first principles.⁵⁷

The four-parameter fit at room temperature also yielded the parameters $\epsilon_s = 14.0$ and $\epsilon_\infty = 5.0$, where the high-frequency dielectric constant has been deduced from fits of the reflectivity up to $2,000\text{ cm}^{-1}$ (see, e.g., Fig. 4). The static dielectric constant compares well to our dielectric result, $\epsilon_s = 14.2$, or to literature, where a value of 12.9 (Ref. 39) is reported. It is important to note, that in the four-parameter fit the Lyddane-Sachs Teller relation is automatically fulfilled and the static dielectric constant follows from the dielectric strength of the observed phonon mode. It seems that specifically the dielectric strength and concomitantly the longitudinal optical phonon frequency is at odds with the values reported in literature.⁵³ From the dielectric strength the ionic plasma frequency can be directly calculated. Assuming ideal ionic bonding with valences of $Z = \pm 2$ we expect an ionic plasma frequency of 2040 cm^{-1} [see Eq. (6)]. This has to be compared with the experimentally observed room temperature value of the ionic plasma frequency which amounts, $\Omega = 987\text{ cm}^{-1}$. This value is very close to the one observed in MnO, where $\Omega = 1077\text{ cm}^{-1}$ has been determined.⁸ It indicates strong covalent contributions to the bonding in CoO. Specifically, the effective valence is found to be $Z^* = 1.0$, much lower than the ideal ionic valence of $Z = 2$. From γ -ray diffraction it has been concluded that the Co-O interaction is purely ionic.⁵⁵

B. Electronic excitations

1. Splittings of the Co^{2+} ground state

Now, we want to turn to the additional excitation features that are visible in Figs. 4 and 5. The frequencies derived from our reflectivity measurements are listed in Table II and compared to excitation energies observed in FIR transmission, Raman, and neutron scattering experiments. Evidently, many correspondences between our excitation frequencies and the ones in literature can be found. Before we discuss in detail the approaches sug-

TABLE II: Electric quadrupole (Q_i) and magnetic dipole (M_i) excitations in CoO observed in the present work. Listed are also electronic resonances and magnon excitations reported in previous far-infrared absorption, Raman, and neutron scattering investigations together with the temperatures these experiments were performed at. All eigenfrequencies are given in cm^{-1} .

| reflectivity (this work) | FIR | | | Raman | | neutron scattering | | |
|-----------------------------|---------|---------|---------|---------|---------|--------------------|---------|--------------------|
| | Ref. 30 | Ref. 31 | Ref. 32 | Ref. 52 | Ref. 58 | Ref. 54 | Ref. 59 | Ref. 60 |
| 8 K | 2 K | 4.2 K | 10 K | 20 K | 10 K | 110 K | 10 K | 6 K, (1.5 1.5 0.5) |
| $\sim 142(M_1)$ | 142.3 | | 146 | 143 | 143 | 145-178 | | 163 |
| | 146.5 | | | 148 | | | | |
| 220(Q_1) | | 216 | 215 | | | 214-245 | 218 | |
| 221(M_2) | | 221 | 221.5 | 221 | 221 | | | 216 |
| | | | 233 | | | | | |
| | | | 243 | | | | | |
| 250(M_3) | | 248 | 250 | | | | | 253 |
| | | | 260 | | | | | |
| 295(M_4) | | | 296 | 296 | 296 | 340-350 | 313 | 315 |
| 600(Q_2) | | | | | 530(?) | | | |
| 680(Q_3) | | | | | | | | |

gested to describe these excitations, we want to address the fact that a first distinction between the Q_1 - Q_3 and the M_1 - M_4 excitations can directly be made from the reflectivity data. Looking at Eq. 1 one can see that a contribution to the magnetic permeability $\mu(\omega)$ like, for example, magnetic dipole (MD) transitions can lead to a reduction of the reflectivity and may produce a dip-like feature in the spectrum. MD transition between d states are symmetry-allowed, but usually are very weak with an oscillator strength of 10^{-6} and their contribution to $\mu(\omega)$ does not show up in optical spectra. The situation changes, however, when AFM order sets in and $\mu(\omega)$ reaches values which become comparable to $\varepsilon(\omega)$. The transitions M_1 - M_4 fit well to such a scenario, showing dip-like features in the reflectivity and appearing only below a temperature of about 100 K, deeply in the AFM phase. Therefore, we assign these features to MD transitions. Note that similar observations of MD transition have been reported by Häusler *et al.*⁶¹ for the related compound CoF₂, where Co has the same electronic configuration as in CoO. While $M_1 - M_4$ only appear far below T_N , the peak-like transitions $Q_1 - Q_3$ do not show any significant changes at T_N and are, obviously, not related to $\mu(\omega)$ but contribute to $\varepsilon(\omega)$. It is clear that on-site electric dipole transitions between the Co d -states are parity forbidden, but can become allowed when the mixing with phonons breaks the inversion symmetry. Such a mechanism, however, should result in a characteristic temperature dependence^{29,62,63,64}, which is not observed. Therefore, we assign the transition $Q_1 - Q_3$ to electric quadrupole transitions, which are symmetry allowed with an expected oscillator strength of about 10^{-6} , the same order of magnitude as the MD transitions.

Let us now turn to the expected level scheme (see Fig. 8) for Co²⁺ ions in CoO. Following Liehr,⁶⁵ who

described the three-electron-hole cubic ligand-field spectrum in full detail, we can assign the lower two eigenstates, at 220 and 600 cm^{-1} , to transitions between the $^4F_{9/2}$ ground state which is split by the spin orbit coupling. The energy level at 680 cm^{-1} , obviously arises from a transition of the ground state to an excited one which is derived from the $^4F_{7/2}$ state. Liehr⁶⁵ deduced his results taking into account SOC in the atomic limit and then switching on the crystal field. Usually, the crystal field splitting is calculated from the atomic limit and then SOC is introduced. In this case and assuming only the lowest crystal field components, the crystal-field ground state splits into three levels only, the two highest levels being degenerate. Having made these qualitative assignments, we will now substantiate our conclusions by analyzing the energy level scheme of the high-spin Co²⁺ ion following the approach by Sakurai *et al.*⁵⁴ To describe the energy splittings of the groundstate above T_N we will take into account only SOC, while in the AFM phase an additional tetragonal crystal field and the effects of exchange splitting have to be considered. Hence, our starting Hamiltonian for the ground state is given by

$$H = \lambda(\mathbf{S}\mathbf{L}) + D[3L_z^2 - L(L+1)] + 6J\langle\alpha\mathbf{S}\rangle(\alpha\mathbf{S}), \quad (9)$$

where λ denotes the SOC constant, D is the tetragonal CF parameter, and the last term is the nearest neighbor exchange coupling. We want to recall some features of the superexchange interaction of Co²⁺ ions via oxygen in Co-O-Co fragments (for short we are using the hole representation $t_{2g}e_g^2$). From a general point of view, one can distinguish the following exchange parameters: J_{ee} between e_g^2 sub-shells, J_{tt} between t_{2g} holes, and J_{te} between e_g^2 and t_{2g} sub-systems (this statement is based on the internal symmetry of the exchange Hamiltonian; for details see Ref. 66). Note that the e_g^2 sub-shells are half

filled and that therefore the effective orbital momentum vanishes. Hence, the leading term in the superexchange interaction of the Co ions can be written in the Heisenberg form in first approximation, i.e., $H_{ab}^{\text{ex}} \approx J(\mathbf{S}_a \mathbf{S}_b)$, where \mathbf{S}_a and \mathbf{S}_b are the total spins of the e_g^2 sub-shell of the ion at site a and b , respectively. The exchange parameters were constrained to one J since J_{ee} is dominating. Furthermore, it is possible to introduce an effective orbital momentum \mathbf{L} with $L = 1$ for the $\text{Co}^{2+}({}^4\Gamma)$ state as well as an effective total momentum $\mathbf{j} = \mathbf{L} + \mathbf{S}$ (see Refs. 41 and 54). Using the wave functions $|j, m_j\rangle$, listed in Ref. 41, where m_j is the quantum number of the component of \mathbf{j} along the axis of quantization, it is straightforward to deduce the energy spectrum $\epsilon(j, m_j)$ of the $\text{Co}^{2+}({}^4\Gamma)$ state in crystal and molecular exchange fields:

$$\begin{aligned}
\epsilon\left(\frac{1}{2}, \pm\frac{1}{2}\right) &= \pm\frac{25}{6}J, \\
\epsilon\left(\frac{3}{2}, \pm\frac{3}{2}\right) &= \frac{3}{2}\lambda \pm \frac{11}{2}J - \frac{4}{5}D, \\
\epsilon\left(\frac{3}{2}, \pm\frac{1}{2}\right) &= \frac{3}{2}\lambda \pm \frac{11}{6}J + \frac{4}{5}D, \\
\epsilon\left(\frac{5}{2}, \pm\frac{5}{2}\right) &= 4\lambda \pm \frac{15}{2}J + D, \\
\epsilon\left(\frac{5}{2}, \pm\frac{3}{2}\right) &= 4\lambda \pm \frac{9}{2}J - \frac{1}{5}D, \\
\epsilon\left(\frac{5}{2}, \pm\frac{1}{2}\right) &= 4\lambda \pm \frac{3}{2}J - \frac{4}{5}D
\end{aligned} \tag{10}$$

These analytical expressions are very useful as a starting point for calculations, however, they have to be corrected, since the axis of magnetization in CoO is not parallel to the tetragonal one. This leads to the last term in Eq. 9. To date, the values α are still under debate (see Ref. 28), however, in most publications^{31,58} it is believed that the spins point into the $[\bar{1}\bar{1}7]$ direction. Hence we set $\alpha = \frac{1}{\sqrt{51}}(-1, -1, 7)$. The experimentally observed magnetic dipole transitions listed in Tab. II and located at 142, 221, 249, and 295 cm^{-1} were fitted using Eq. 9 with the SOC parameter λ , the crystal field parameter D and the magnetic exchange J as free parameters. In these calculations we assumed that only transitions from the ground state $\epsilon(1/2, -1/2)$ were observed and that we detect all possible transitions with $\Delta m_j = 0, \pm 1$. The best fit resulted in a levels scheme $\epsilon(1/2, -1/2) = 0 \text{ cm}^{-1}$, $\epsilon(1/2, +1/2) = 145.7 \text{ cm}^{-1}$, $\epsilon(3/2, -3/2) = 221.9 \text{ cm}^{-1}$, $\epsilon(3/2, -1/2) = 248.8 \text{ cm}^{-1}$, and $\epsilon(3/2, +1/2) = 294.3 \text{ cm}^{-1}$ which is shown in Fig. 8. This calculated level scheme is very close to the experimentally observed magnetic excitations and resulted in parameters $\lambda = 151.1 \text{ cm}^{-1}$, $J = 17.5 \text{ cm}^{-1}$, and $D = -47.8 \text{ cm}^{-1}$. The transition to the level $\epsilon(3/2, +3/2) = 432.9 \text{ cm}^{-1}$ is magnetic dipole forbidden and, therefore, can not be observed in our experiment.

Having derived the splitting parameters in the AFM state by fitting the energies of the MD transitions, we have to compare these parameters to the energies of the transitions $Q_1 - Q_3$ which are also present above

the AFM transitions. We identify these transitions as electric quadrupole transitions between the spin-orbit split crystal field states. Note that transitions from the ground to the excited states with effective moment $j = 5/2 \Leftrightarrow \Gamma_7, \Gamma_8$ are allowed only via electric quadrupole mechanisms. This explains why the optical transitions near 600 and 680 cm^{-1} are not sensitive to the change of $\mu(\omega)$ upon the phase transition into the antiferromagnetic state. As can be seen from Eq. 10 by assuming $J = D = 0$ the level separation between the ground state and the first excited state above T_N is given by $3/2\lambda$. In CoO this immediately results in a SOC constant $\lambda = 146.7 \text{ cm}^{-1}$, in good agreement with the SOC parameter derived from the MD transition at low temperatures. To handle the slight discrepancies between calculation and observed energies, a detailed inspection of the corrections due to $t_{2g}-e_g^2$ and $t_{2g}-t_{2g}$ exchange interactions and the orthorhombic crystal field is necessary, which is out of the scope of the present paper.

2. Higher-lying CF excitations

Higher-lying CF excitations have been determined from optical absorption by Pratt and Coelho.²⁹ They found two prominent absorption lines close to 8,000 and 18,500 cm^{-1} . At low temperatures the high-energy transition revealed some substructure. These transitions were identified as transitions from the 4F_1 ground state to the 4F_2 and 4F_1 excited states, which results in a crystal field parameter of approximately $Dq = 900 \text{ cm}^{-1}$. Our results are shown in Fig. 7. In the frequency-dependent dielectric loss as determined from the reflectivity, these transitions can only be detected by a close inspection of our spectra. Slight maxima, which are almost tem-

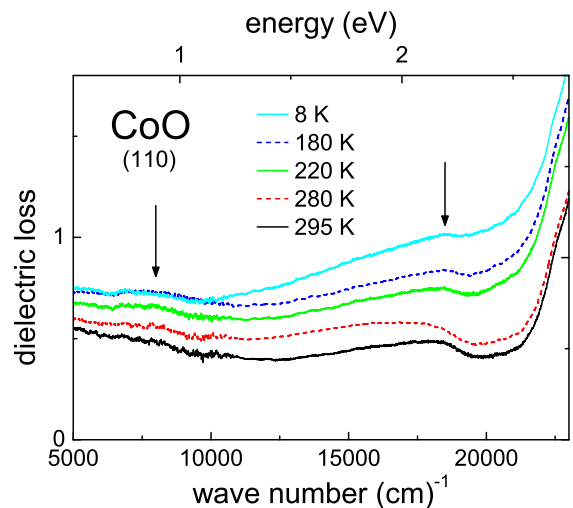


FIG. 7: (Color online) Dielectric loss vs. wave numbers for CoO between 5,000 and 23,000 cm^{-1} . Electronic $d-d$ excitations are indicated by arrows.

perature independent and show no significant changes at the magnetic phase transition, appear close to 8,000 and 18,500 cm^{-1} . Beyond 21,000 cm^{-1} ($= 2.6 \text{ eV}$) the dielectric loss strongly increases, entering the frequency regime of strong absorption. The crystal field excitations are broad and very weak in intensity and do not show any detectable splittings due to SOC effects. It is clear that these $d-d$ excitations are parity forbidden and gain intensity only via hybridization with other electronic orbitals or via coupling to phonons.

It is interesting to note that the optical gap as determined from the transport measurements rather coincides with the lower band edge of the 18,500 cm^{-1} transition, which can be located close to 12,000 $\text{cm}^{-1} \sim 1.5 \text{ eV}$. It is however unclear, how this on-site excitation can contribute to the dc hopping transport. The most plausible explanation of the transport gap certainly is the formation of an impurity band due to defects.

V. SUMMARY AND CONCLUDING REMARKS

We performed a careful characterization of single crystalline CoO, utilizing magnetic and dielectric susceptibility, as well as thermodynamic measurements. We determined the phase transition into the AFM state as $T_N = 289 \text{ K}$. The low temperature heat capacity can well be described by a T^3 law with a Debye temperature $\Theta_D = 451 \text{ K}$. It seems that at low temperatures magnetic excitations play a minor role and do not contribute to c_p . This can be understood from the electronic excitations, with a series of levels between 150 and 300 cm^{-1} at low T . It documents that SOC is strong compared to the magnetic exchange. From dielectric spectroscopy we determined $\varepsilon_s = 14.2$ and an electronic gap from the dc transport $E_g = 1.5 \text{ eV}$.

We analyzed the phonon dynamics including the spin-phonon coupling at the antiferromagnetic ordering temperature. Damping and eigenfrequencies can be described by a normal anharmonic behavior. However, below T_N a second mode splits off. The splitting amounts to 15.0 cm^{-1} at low temperatures, considerably lower than in the case of the isostructural antiferromagnet MnO. This behavior might be explained taking the strong frustration of MnO into account, while in CoO Néel temperature and Curie-Weiss temperature are of the same order of magnitude. The ionic plasma frequency amounts to about 980 cm^{-1} , signaling considerable covalent bonding.

In the second part of this work we determined the electronic and magnetic transitions. The measured reflectivity allows to discriminate between electric and magnetic dipole transitions. The complete level scheme of the electronic excitation spectrum of CoO is plotted in Fig. 8. Starting from the electronic levels we determined two crystal field excitations close to 8,000 and 18,500 cm^{-1} . From these excitations we determine a crystal field parameter $Dq = 900 \text{ cm}^{-1}$, in good agree-

ment with values reported from infrared absorption.²⁹ These transitions are spin allowed transitions where only one electron from the t_{2g} ground state ($t_{2g}^5 e_g^2$) is excited into an e_g level ($t_{2g}^4 e_g^3$). In CoO SOC effects are strong and have to be taken into account. We determined the splitting of the crystal field ground state by SOC and identified three excited levels. From the separation of the first two levels we determine the SOC constant $\lambda = 146.7 \text{ cm}^{-1}$. This value is reasonable compared to the free ion case where $\lambda_{\text{Ion}} = 176 \text{ cm}^{-1}$.⁴¹ Due to the tetragonal distortion, Γ_7 and Γ_8 are not degenerate but are separated by 80 cm^{-1} . In the free ion case these levels are degenerate and the separation from the ground state amounts 4λ . Hence in the atomic limit we would expect one excitation at 606 cm^{-1} , instead of two excitations at 600 and 680 cm^{-1} , which we identified in CoO, in a crystal with strong covalent bonding. Finally, we determined a series of magnetic dipole excitations at 142, 221, 249, and 295 cm^{-1} , which can clearly be identified as magnetic dipole transitions between the spin-orbit split crystal field levels whose degeneracy is completely lifted by molecular exchange fields in the AFM state. The levels for the lowest doublet and the first excited quartet are also indicated in Fig. 8. These transitions appear at low temperatures ($< 100 \text{ K}$), are very weak, and exhibit almost no temperature dependence. We were able to describe the experimentally observed level scheme convincingly by a model taking the SOC parameter $\lambda = 151.1 \text{ cm}^{-1}$, the magnetic exchange $J = 17.5 \text{ cm}^{-1}$, and the tetragonal crystal field parameter $D = -47.8 \text{ cm}^{-1}$ into account. The calculated energy levels are also displayed in Fig. 8.

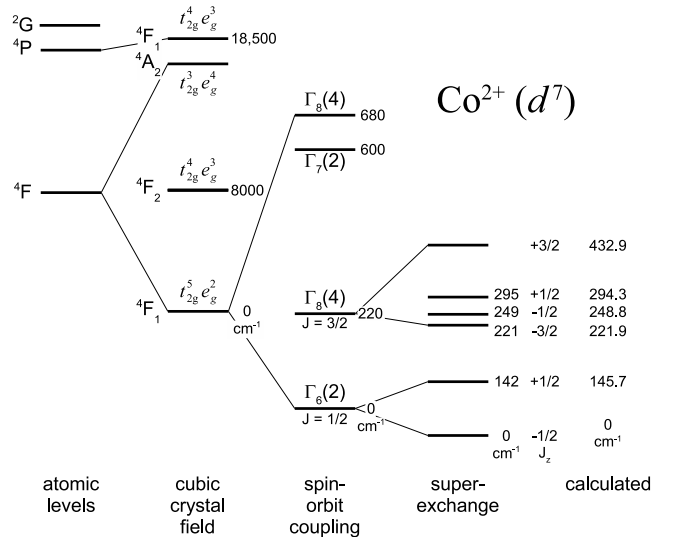


FIG. 8: Schematic splitting of the energy levels of the Co²⁺ ion in CoO. The energies are given in cm^{-1} as determined in the present work. The magnetic dipole transitions only appear below 100 K, deep in the magnetically ordered phase. Note that different energy scales are used to display the effects of different interactions.

In conclusion, we were able to determine the complete phonon, electronic and magnetic excitation spectrum of CoO within the charge-transfer gap by infrared spectroscopy. CoO is a prototypical and well known example for a strongly correlated system, but its phononic, electronic, and magnetic excitation schemes offers an astonishing complexity.

Acknowledgments

This research has partly been supported by the Deutsche Forschungsgemeinschaft DFG, via the Collaborative Research Center SFB 484 (University of Augsburg).

-
- ¹ A. Gorschluter and H. Merz, Phys. Rev. B **49**, 17293 (1994).
- ² B. C. Larson, W. Ku, J. Z. Tischler, C.-C. Lee, O. D. Restrepo, A. G. Eguiluz, P. Zschack, and K. D. Finkelstein, Phys. Rev. Lett. **99**, 026401 (2007).
- ³ M. W. Haverkort, A. Tanaka, L. H. Tjeng, and G. A. Sawatzky, Phys. Rev. Lett. **99**, 257401 (2007).
- ⁴ J. Zaanen, G. A. Sawatzky, and J. W. Allen, Phys. Rev. Lett. **55**, 418 (1985).
- ⁵ S. Massidda, M. Posternak, A. Baldereschi, and R. Resta, Phys. Rev. Lett. **82**, 430 (1999).
- ⁶ W. D. Luo, P. H. Zhang, and M. L. Cohen, Solid State Commun. **142**, 504 (2007).
- ⁷ E. M. L. Chung, D. M. Paul, G. Balakrishnan, M. R. Lees, A. Ivanov, and M. Yethiraj, Phys. Rev. B **68**, 140406(R) (2003).
- ⁸ T. Rudolf, Ch. Kant, F. Mayr, and A. Loidl, Phys. Rev. B **77**, 024421 (2008).
- ⁹ A. B. Sushkov, O. Tchernyshyov, W. Ratcliff II, S. W. Cheong, and H. D. Drew, Phys. Rev. Lett. **94**, 137202 (2005).
- ¹⁰ T. Rudolf, Ch. Kant, F. Mayr, J. Hemberger, V. Tsurkan, and A. Loidl, Phys. Rev. B **75** (2007); J. Hemberger, T. Rudolf, H. A. K. von Nidda, F. Mayr, A. Pimenov, V. Tsurkan, and A. Loidl, Phys. Rev. Lett. **97** (2006); T. Rudolf, Ch. Kant, F. Mayr, J. Hemberger, V. Tsurkan, and A. Loidl, New J. Phys. **9** (2007); J. Hemberger, H. A. K. von Nidda, V. Tsurkan, and A. Loidl, Phys. Rev. Lett. **98** (2007).
- ¹¹ R. V. Aguilar, A. B. Sushkov, Y. J. Choi, S.-W. Cheong, and H. D. Drew, Phys. Rev. B **77**, 092412 (2008).
- ¹² Y. Yamashita and K. Ueda, Phys. Rev. Lett. **85**, 4960 (2000).
- ¹³ O. Tchernyshyov, R. Moessner, and S. L. Sondhi, Phys. Rev. Lett. **88**, 067203 (2002); O. Tchernyshyov, R. Moessner, and S. L. Sondhi, Phys. Rev. B **66**, 064403 (2002).
- ¹⁴ W. Klemm and W. Schüth, Z. anorg. allg. Chemie **210**, 33 (1933).
- ¹⁵ C. H. La Blanchetais, J. Phys. Radium **12**, 765 (1951).
- ¹⁶ J. R. Singer, Phys. Rev. **104**, 929 (1956).
- ¹⁷ T. R. McGuire and W. A. Crapo, J. Appl. Phys. **33**, 1291 (1962).
- ¹⁸ E. Uchida, T. Nagamiya, H. Kondoh, Y. Nakazumi, T. Takeda, and N. Fukuoka, J. Phys. Soc. Jpn. **19**, 2088 (1964).
- ¹⁹ P. S. Silinsky and M. S. Seehra, Phys. Rev. B **24**, 419 (1981).
- ²⁰ N. C. Tombs and H. P. Rooksby, Nature **165**, 442 (1950).
- ²¹ S. Saito, K. Nakahiga, and Y. Shimomur, J. Phys. Soc. Jpn. **21**, 850 (1966).
- ²² W. Jauch, M. Reehuis, H. J. Bleif, F. Kubanek, and P. Pattison, Phys. Rev. B **64**, 052102 (2001).
- ²³ C. G. Shull, W. A. Strauser, and E. O. Wollan, Phys. Rev. **83**, 333 (1951).
- ²⁴ W. L. Roth, Phys. Rev. **110**, 1333 (1958).
- ²⁵ W. L. Roth, Phys. Rev. **111**, 772 (1958).
- ²⁶ B. van Laar, Phys. Rev. **138**, A584 (1965).
- ²⁷ D. Herrmann-Ronzaud, P. Burlet, and J. Rossat-Mignod, J. Phys. C **11**, 2123 (1978).
- ²⁸ E. Ressouche, N. Kernavanois, L.-P. Regnault, and J.-Y. Henry, Physica B **385-386**, 394 (2006).
- ²⁹ G. W. Pratt and R. Coelho, Phys. Rev. **116**, 281 (1959).
- ³⁰ R. C. Milward, Phys. Lett. **16**, 244 (1965).
- ³¹ M. R. Daniel and A. P. Cracknel, Phys. Rev. **177**, 932 (1969).
- ³² I. G. Austin and E. S. Garbett, J. Phys. C: Solid State Phys. **3**, 1605 (1970).
- ³³ U. Schneider, P. Lunkenheimer, A. Pimenov, R. Brand, and A. Loidl, Ferroelectrics **249**, 89 (2001).
- ³⁴ M. B. Salamon, Phys. Rev. B **2**, 214 (1970); M. B. Salamon, P. R. Garnier, B. Golding, and E. Buehler, J. Phys. Chem. Solids **35**, 851 (1974).
- ³⁵ M. Massot, A. Oleaga, A. Salazar, D. Prabhakaran, M. Martin, P. Berthet, and G. Dhahlenne, Phys. Rev. B **77**, 134438 (2008).
- ³⁶ E. G. King, J. Am. Chem. Soc. **79**, 2399 (1957); E. G. King and A. U. Christensen, *ibid.* **80**, 1800 (1958).
- ³⁷ H. Watanabe, Thermochim. Acta **218**, 365 (1993).
- ³⁸ E. N. Abarra, K. Takano, F. Hellman, and A. E. Berkowitz, Phys. Rev. Lett. **77**, 3451 (1996).
- ³⁹ K. V. Rao and A. Smakula, J. Appl. Phys. **36**, 2031 (1965).
- ⁴⁰ N. Tristan, V. Zestrea, G. Behr, R. Klingeler, B. Buchner, H. A. K. von Nidda, A. Loidl, and V. Tsurkan, Phys. Rev. B **77**, 094412 (2008).
- ⁴¹ A. Abragam and B. Bleaney, *Electron Paramagnetic Resonance of Transition Ions* (Oxford University Press, 1970).
- ⁴² M. S. Kushwaha, Physica B & C **112**, 232 (1982).
- ⁴³ G. Assayag and H. Bizette, Compt. Rend. **239**, 238 (1954).
- ⁴⁴ S. R. Elliott, Adv. Phys. **36**, 135 (1987).
- ⁴⁵ P. Lunkenheimer, V. Bobnar, A. V. Pronin, A. I. Ritus, A. A. Volkov, and A. Loidl, Phys. Rev. B **66**, 052105 (2002).
- ⁴⁶ P. Lunkenheimer, M. Resch, A. Loidl, and Y. Hidaka, Phys. Rev. Lett. **69**, 498 (1992); P. Lunkenheimer, A. Loidl, C. R. Ottermann, and K. Bange, Phys. Rev. B **44**, 5927 (1991); A. Seeger, P. Lunkenheimer, J. Hemberger, A. A. Mukhin, V. Y. Ivanov, A. M. Balbashov, and A. Loidl, J. Phys.: Condens. Matter **11**, 3273 (1999); P. Lunkenheimer and A. Loidl, Phys. Rev. Lett. **91**, 207601 (2003).
- ⁴⁷ F. Gervais and B. Piriou, Phys. Rev. B **10**, 1642 (1974).
- ⁴⁸ J. F. Scott, Phys. Rev. B **4**, 1360 (1971).
- ⁴⁹ A. Kuzmenko, *RefFIT*, University of Geneva, URL <http://optics.unige.ch/alexey/reffit.html>.

- ⁵⁰ R. A. Cowley, *Adv. Phys.* **12**, 421 (1963).
- ⁵¹ K. S. Upadhyay and R. K. Singh, *J. Phys. Chem. Solids* **35**, 1175 (1974).
- ⁵² R. R. Hayes and C. H. Perry, *Solid State Commun.* **14**, 173 (1974).
- ⁵³ P. J. Gielisse, J. N. Plendl, L. C. Mansur, R. Marshall, S. S. Mitra, R. Mykolajewycz, and A. Smakula, *J. Appl. Phys.* **36**, 2446 (1965).
- ⁵⁴ J. Sakurai, W. J. L. Buyers, R. A. Cowley, and G. Dolling, *Phys. Rev.* **167**, 510 (1968).
- ⁵⁵ W. Jauch and M. Reehuis, *Phys. Rev. B* **65**, 125111 (2002).
- ⁵⁶ B. R. K. Gupta and M. P. Verma, *J. Phys. Chem. Solids* **38**, 929 (1977).
- ⁵⁷ U. D. Wdowik and K. Parlinski, *Phys. Rev. B* **75**, 104306 (2007).
- ⁵⁸ H.-h. Chou and H. Y. Fan, *Phys. Rev. B* **13**, 3924 (1976).
- ⁵⁹ K. Tomiyasu and S. Itoh, *J. Phys. Soc. Jpn.* **75**, 084708 (2006).
- ⁶⁰ Z. Yamani, W. Buyers, R. Cowley, and D. Prabhakaran, *Physica B* **403**, 1406 (2008).
- ⁶¹ K. M. Häussler, A. Lehmeyer, and L. Merten, *Phys. Stat. Sol. B* **111**, 513 (1982).
- ⁶² Y. Tanabe and S. Sugano, *J. Phys. Soc. Jpn.* **9**, 753 (1954).
- ⁶³ A. D. Liehr and C. J. Ballhausen, *Phys. Rev.* **106**, 1161 (1957).
- ⁶⁴ J. Deisenhofer, I. Leonov, M. V. Eremin, Ch. Kant, P. Ghigna, F. Mayr, V. V. Iglamov, V. I. Anisimov, and D. van der Marell, arXiv:0809.0666v1 (unpublished).
- ⁶⁵ A. D. Liehr, *J. Phys. Chem.* **67**, 1314 (1963).
- ⁶⁶ M. V. Eremin and Y. V. Kakitin, *Phys. Stat. Sol. B* **82**, 221 (1977).